Received: 12 February 2018 | Accepted: 29 April 2018
DOI: 10.1002/suco.201800042

TECHNICAL PAPER

Uniaxial and lateral strain behavior of ribbed reinforcement bars inspected with digital image correlation

Haukur J. Eiriksson[1] | Bjarni Bessason[1] | Runar Unnthorsson[2]

[1]Faculty of Civil and Environmental Engineering, University of Iceland, Reykjavík, Iceland
[2]Faculty of Industrial Engineering, Mechanical Engineering and Computer Sciences, University of Iceland, Reykjavík, Iceland

Correspondence
Haukur J. Eiríksson, Faculty of Civil and Environmental Engineering, University of Iceland, Hjardarhagi 2-6, 107 Reykjavík, Iceland.
Email: haukurj@hi.is

Funding information
Eimskip University Fund of the University of Iceland; Ludvigs Storr Trust Fund; University of Iceland Research Fund

Knowledge about the plastic behavior of reinforcement steel bars in reinforced concrete (RC) structures is important, especially for seismic design. This paper presents the results of experimental tests where the main aim was to map the plastic deformations of long ribbed reinforcement bars, both in the axial and lateral directions, in order to provide useful information about the behavior of reinforcement bars inside concrete. The study showed that the digital image correlation (DIC) technique is very suitable for this kind of tests. The uniaxial stress–strain curves for side-by-side and different gauge lengths (1d, 3d, 5d, 10d) were identical all the way to the max stress, but after that the segment including the neck dominated the strain development. The Poisson's ratio increased rapidly during the yielding phase to 0.44–0.49 and was constant all the way to rupture. The location of the neck could be predicted at the end of the yielding phase.

KEYWORDS
DIC, experimental observation, gauge lengths, lateral strain, Lüder's behavior, necking, Poisson's ratio, ribbed reinforcement bars, stress–strain curves, uniaxial strain

1 | INTRODUCTION

Seismic design of reinforced concrete (RC) buildings in earthquake prone areas presumes nonlinear behavior and energy dissipation. Generally, nonlinear behavior of RC structural elements can be caused by cracking of concrete, plastic compression deformations, and crushing of the concrete and plastic deformations of the reinforcement.[1] Other nonlinearity arises from bond slip between steel and concrete, aggregate interlock of cracked concrete, and dowel action. In seismic design, brittle failure modes are not desirable, while ductility and plastic deformations of the reinforcement play an important role in energy dissipation.[2]

Nonlinear behavior of RC elements is known to be complicated and experimental work is needed to support and develop reliable computational models. This requires destructive testing where the test specimens are loaded until failure. Such testing includes the risk of damaging conventional meters and sensors that are directly connected to the specimens, especially test specimens made of concrete. Fortunately, other non-contacting measurement techniques are available. One of them is a full field non-contact optical technique known as digital image correlation (DIC). The main principle of the method is to match a selected facet on the surface of the specimen before and after a load step and thus follow the deformations. The method can detect deformations anywhere on the surface of the specimen which is facing the camera(s).

The DIC technology has been applied for more than three decades. It was originally proposed by a group of researchers at the University of South Carolina, United States, early in the

Discussion on this paper must be submitted within two months of the print publication. The discussion will then be published in print, along with the authors' closure, if any, approximately nine months after the print publication.

1980s.[3,4] Since then the method has been developed and refined and the algorithms have been improved.[5,6] DIC measurements can be carried out using one camera or two cameras, from which two and three-dimensional (2D/3D) displacements and strains can, respectively, be calculated.[6] Improvements in digital camera technology in recent decades, for example, higher resolution, have facilitated improvements in DIC analysis. The DIC methodology is now an accepted method to measure surface displacement and the application field is quite broad. It has successfully been used to study cracks in masonry walls,[7] bond behavior of fiber reinforced polymers (FRPs) bonded to masonry,[8] shear stresses of FRP strengthened RC beams,[9] size effect on shear strength of RC beams,[10] shear capacity and mechanical behavior of prestressed concrete beams,[11] and shear connection of precast RC structural walls,[12] among other uses. Additionally, the method has also been used to compute mechanical properties of materials.[13,14] These studies and many others have shown that the accuracy is satisfactory and often better than can be expected with traditional techniques. The accuracy depends on the resolution of the camera used, the distance from camera to specimen, and by the fines and details of the pattern on the surface of the test specimen. The quality of the processing algorithms and software used to correlate the images is also very important. However, the method can have some limitations when monitoring RC elements, for instance in the case of spalling of the concrete surface.[15]

Knowledge of the main characteristics of plastic behavior of reinforcement steel bars is important when modeling the nonlinear behavior of RC elements, especially in structures in seismic zones where ductile and inelastic behavior of the reinforcement is required. Standard uniaxial stress–strain curves for steel bars are based on laboratory tests of 5d (d is the diameter of the steel bar) long specimens,[16] and the question is how do they reflect the actual behavior of long reinforcement bars inside the concrete in the failure zones of RC elements? This study of reinforcement bars is a part of a test series containing concrete test specimens including ribbed reinforcement bars with 10 mm diameter.

In this study experimental work was carried out for engineering purposes to investigate the uniaxial and lateral strain of "long" reinforcement steel bars (i.e., longer than the standard length of 5d) in both elastic and plastic phases, using a uniaxial tension test, with the main focus on the plastic phase. The single camera 2D DIC technique was used to map deformations. No references were found about this subject in a literature survey. The main research questions were:

- How do the uniaxial stress–strain behaviors for 1d, 3d, 5d, and 10d gauge lengths differ from each other?
- How does the stress–strain behavior of adjacent gauge segments compare to the main gauge segment that includes the neck?
- What is the development of the Poisson's ratio from the elastic phase to rupture?

The information obtained from the tests is believed valuable for earthquake and structural engineers when designing RC structural elements in seismic zones.

2 | MATERIALS AND TEST SETUP

2.1 | Specimen preparation and camera setup

A trial and error method for specimen preparation and camera setup was necessary to succeed with the experiments. The mill scale was removed by washing the steel bars with hydrochloric acid (HCl) and the bars were primed with a thin layer of matte white spray paint. Black dots were marked manually with a pen (Figure 1).

Resolution of the camera is a key factor in a successful DIC analysis. In this study a 36-megapixel camera was used. The focus of the camera was kept fixed during each test to avoid artificial strains. Furthermore, rocking of the camera back and forth or movement of the test specimen toward or away from the camera (i.e., movement perpendicular to the plane of the pictures) affects the strain analysis. The out-of-plane movement was measured in a special test with two cameras (test no. 6, Table 1), where it appeared to be very small and only had a minor effect on the test results. A typical error was approximately 2% for the uniaxial elastic strain, which decreased rapidly with increased strain. To avoid rocking of the camera in this test the top of the tripod was in the lowest position and loaded with a sandbag underneath (Figure 2).

In DIC analysis "subsets" (square boxes) each with a different random pattern are defined and tracked as the specimen moves and deforms (Figure 1c). The displacement of the center of each subset is given in the output results. The size of the subsets must be defined in harmony with the resolution of the pictures and the applied pattern, where several dots are needed inside each subset (Figure 1c). Generally, the size of the subsets in this study was in the range of 1.0 × 1.0 to 1.5 × 1.5 mm. In the DIC analysis "steps" must also be defined, which is the distance between the centers of the subsets which also defines a grid in an *X*–*Y* coordinate system for the output results.

A tape measure located on the same plane as the test specimen was used to determine a scaling factor between the

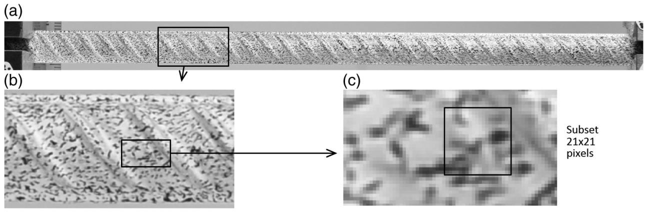

FIGURE 1 (a, b) Example of dots on a $d = 10$ mm bar's surface made manually with a 0.2 mm black pen (bar 5.2). (c) A subset of the size 21 × 21 pixels (1.5 × 1.5 mm) used in the DIC analysis of bar 5.2

TABLE 1 Overview of the reinforcement bars tested, where the bars are numbered with the test number followed by a running number. The free length is the visible part of the bars between the grips of the testing machine

Test and bar no.	Diameter (mm)	Free length (mm)	Resolution of pictures (pixels/mm)	(mm/pixel)	Remarks
1.1, 1.2, 1.3	10	170	21.1	0.047	
2.1, 2.2, 2.3, 2.4	10	775	9.01	0.111	Thickening at the ends
3.1, 3.2	10	775	7.43	0.135	Thickening at the ends
4.1, 4,2	10	775	7.43	0.135	
5.1, 5.2	10	195	14.2	0.070	Different sides, one at a time
5.3	10	195	14.2	0.070	Smooth bar
6.1, 6.2, 6.3	10	195	41.3/27.8	0.024/0.036	Two perpendicular cameras
6.4, 6.5	10	195	41.3/27.8	0.024/0.036	Smooth bars. Two perp. cam.

pixels and the units used, here millimeters, and to correct for lens distortion.

A routine was used to crop the images to reduce their sizes in order to speed up the DIC analysis which was performed with the software DaVis 8 from LaVision.[17]

2.2 | Test setup

The tension test of the bars was executed in an Instron testing machine with a capacity of 500 kN which is especially equipped for execution of tension and compression tests. A 500 kN load cell was used to measure the applied load (Figure 2).

The tests were executed in a displacement controlled mode in order to get a sufficient number of pictures for the DIC analysis for the elastic, yielding, strain-hardening, and descending phases. The speed of the applied tension load was in harmony with both the stress-rate limits in the Eurocode test standard[16] and the frames per second capacity of the camera. In this test one frame per second was used. All pictures taken during the elastic phase were used, all or every second picture during the yielding phase, and every fifth to fifteenth during the strain-hardening and descending phases, resulting in approximately 130–200 pictures that were used in each DIC analysis. This was performed in order to reduce the calculation time and the size of the output files. A monitor showing the jack load was located close to the specimen and visible on all photos and was used for synchronization of the load with the DIC analysis deformations (Figure 2).

2.3 | Test specimens

Table 1 provides an overview of the bars tested, together with the corresponding image resolution. The reinforcement bars have a characteristic yield strength of min 500 MPa and a strain at max stress of min 7.5% according to class C in Eurocode 2.[18] The bars had two rows of transverse ribs and two longitudinal ribs. All the bars fulfilled the demands concerning strength, strain, and geometry according to Eurocode 2[18] and EN 10080:2005.[19]

All the tested bars had a diameter of 10 mm. The “free length” in Table 1 defines the length of the visible part of the bars between the grips of the testing machine. The bars in tests 2 and 3 had a thickening (16 mm steel rod) welded to each end so the length of the ribbed part of the specimens was 600 mm. The purpose with tests 1–4 was to determine the uniaxial stress–strain curves of the bars. During these tests some interesting behavior was observed in the lateral direction, so the test series was extended with tests 5 and 6. The view of the bars in test 5 was rotated 90° in order to measure the ribbed bars from two perpendicular directions (Figure 3), but only from one side at a time as only one camera was used. In test 6 two cameras were used to take photos simultaneously from two perpendicular directions for corrections of out-of-plane movements of the test specimens. The main camera had a 36-megapixel resolution, whereas the second camera had a 12-megapixel resolution. The two cameras were placed closer to the bars than in previous tests in order to increase the resolution of the pictures (Table 1). Additionally, smooth steel bars without ribs (bars no. 5.3, 6.4, and 6.5) were tested for comparison with the ribbed bars. Most of the tested bars developed a neck within the picture frame, except for bar no. 5.1 where the necking occurred inside one of the grips of the testing machine. For

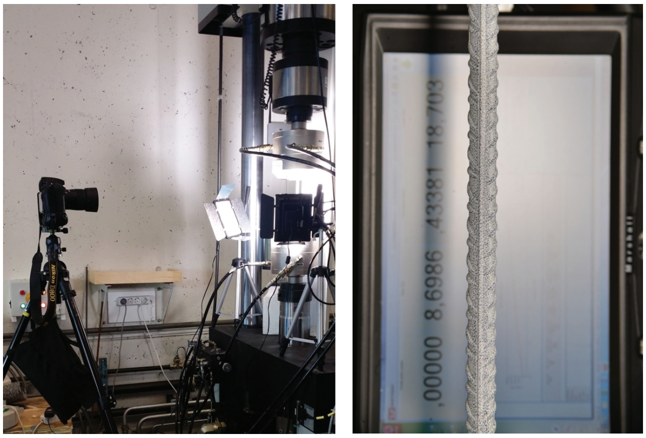

FIGURE 2 (left) Test setup with one camera on a tripod with a sandbag hanging underneath, two LED lamps, and a monitor. (right) Picture of a test specimen and the monitor behind used in the DIC analysis

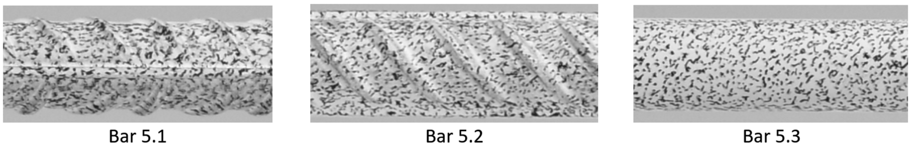
Bar 5.1

Bar 5.2

Bar 5.3

FIGURE 3 Reinforcement bar no. 5.1 had a longitudinal rib facing the camera, while bar no. 5.2 had transverse ribs facing the camera. Bar no. 5.3 was a smooth bar, that is, without ribs

bars no. 6.1, 6.2, 6.5 the neck occurred outside the picture frame, which did not cover the whole free length of the bars in test 6.

3 | LENGTH OF TEST SECTION

3.1 | Uniaxial gauge lengths

A standard length of test section (gauge length) for alloy samples is five times the diameter of the section (5d), that is, 50 mm for 10 mm bars.[16] Test samples are commonly prepared to have one such test section. Using long bars and the DIC method the standard main gauge segment can be located afterward and symmetrically around the neck (Figure 4). Additionally, other gauge segments can be located beside the main gauge segment, that is, side-by-side gauge segments (Figure 4) or by overlapping segments (Figure 5). Furthermore, different gauge lengths can be tested (1d, 3d, 5d, 10d, etc.). This means that the uniaxial strain can be measured anywhere on the bar and with different gauge lengths.

3.2 | Lateral gauge length

No standard procedure for determination of the lateral strain and the Poisson's ratio (the ratio between the lateral and uniaxial strain) of reinforcement bars exist. As for the uniaxial strain the lateral strain can be determined afterward anywhere on a bar's surface. The lateral gauge length is, however, limited to the bar's width. In this study the outermost points along both sides of the bars were used and the distance between them was generally about 8 mm (0.8d). The inaccuracy of the DIC measurements increased with shorter gauge lengths (as for all measurements), which mainly affected the elastic phase where the deformations were small. This can be counteracted by computing average strains for many cross sections in the whole bar. In the plastic phase the inaccuracy of the measurements had negligible effects on the measured strain.

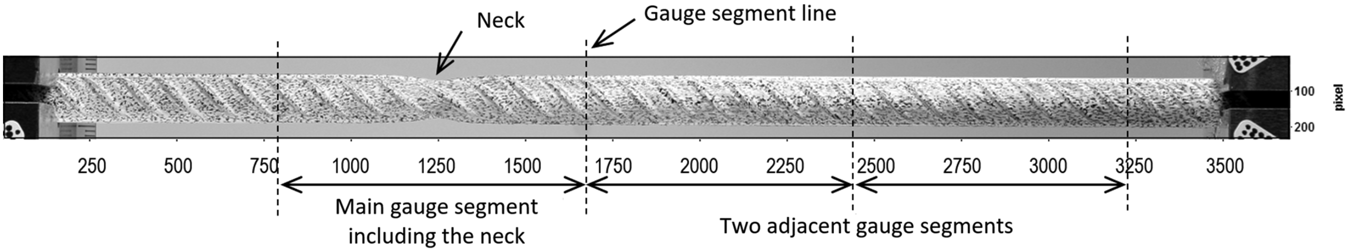

FIGURE 4 Picture of a bar analyzed in DIC just before it ruptured (bar 5.2). The coordinate system has its origin in the top left corner and the axes have pixels as a unit. The main 5d gauge segment has the neck at the center. Two additional side-by-side 5d gauge segments are defined as well

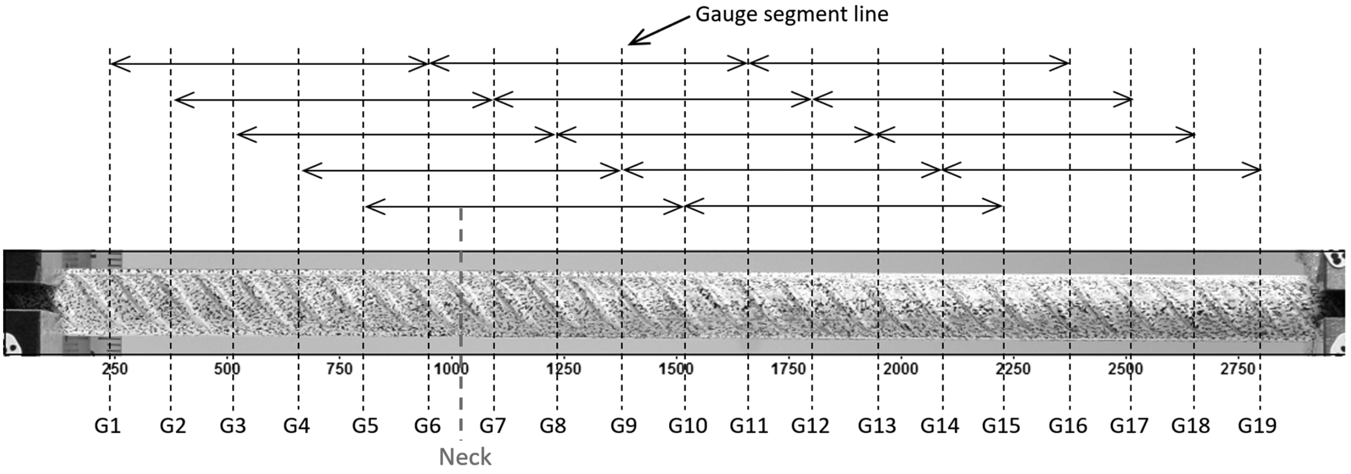

FIGURE 5 Gauge segment lines with 10 mm distance are defined along the bar, G1–G19. This results in fourteen overlapping 5d gauge segments stress–strain curves for bar 5.2. The neck is located between gauge segment lines G6 and G7

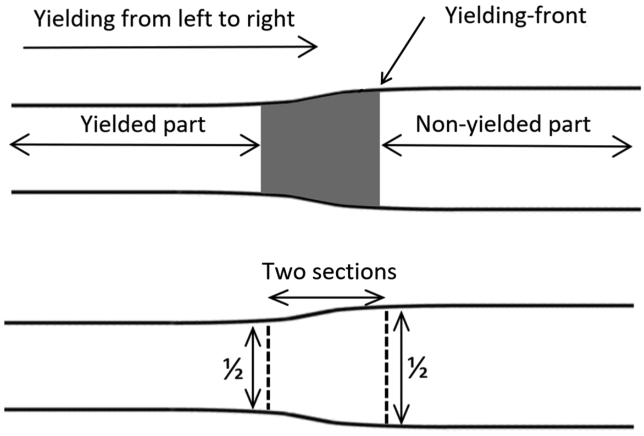

FIGURE 6 Drawing illustrating determination of Poisson's ratio for one-gauge length where an average of the lateral strain is used. Here it is shown for the yielding phase where the yielding propagates from one end of the bar to the other (Lüder's behavior). The active part in yielding is shown in grey

For calculation of Poisson's ratio an average of the lateral strains at both ends of the gauge segment can be used as a representative value for this test section. This works well in the elastic phase and in the strain-hardening phase when the strain development of the steel bar is identical at all locations. However, during the yielding phase the localized yielding-front propagates from one end of the bar to the other, known as Lüder's behavior.[20] When the yielding-front, known as Lüder's band-front, has just passed the first section of a gauge segment (Figure 6), the lateral strain becomes relatively larger than the uniaxial strain measured between the first and the second sections, resulting in too large Poisson's ratio. Similarly, the Poisson's ratio gets too small just before the yielding-front reaches the second section, as the uniaxial strain has increased more than the lateral strain. An average of the lateral strain in the two sections will therefore lead to irrelevant peaks in the Poisson's ratio. When the yielding-front has passed the second section both the axial and the lateral yielding strain are fully developed and therefore also the Poisson's ratio. An alternative approach to compute the Poisson's ratio is to use an average value from many cross sections.

4 | STRESS–STRAIN CURVES

4.1 | Uniaxial stress–strain curves for standard 5d gauge length

An average deformation of several points in each segment line was used to determine the uniaxial strain for the three side-by-side 5d gauge segments (Figure 4) presented in Figure 7. The three gauge segments followed each other through the elastic phase, but then yielded separately because of Lüder's behavior (see inset in Figure 7). The strain curves then gathered at the end of the yielding plateau and the main gauge segment (included the neck) was in the front (i.e., having the largest strain at the end of the yielding plateau), so the location of the neck was already revealed at that point. This behavior was confirmed for all the bars tested in tests 1, 5, and 6 that included a neck captured inside the picture frame. All the gauge segments then entered the strain-hardening phase as one group and ran parallel to each other throughout the strain-hardening phase where the segment including the neck was in front all the time. The segment including the neck reached a strain of 12.9% at max stress while the others reached 10.5 and 11.5% (see an inset in Figure 7). Soon after the maximum stress the strain in the segments which did not include the neck slowed down and turned downward following an unloading elastic slope, while the main segment went through the descending part of the stress–strain curve.

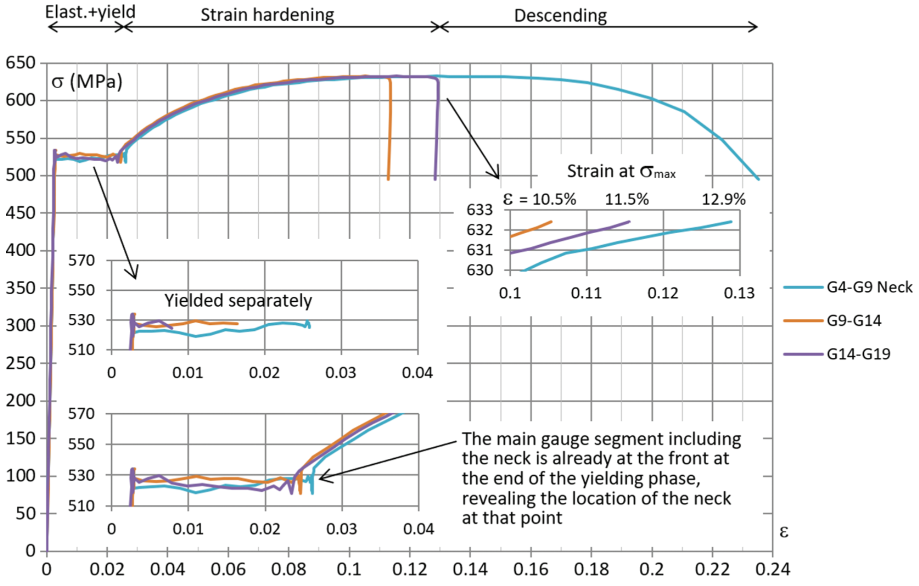

FIGURE 7 Side-by-side stress–strain curves for the 5d gauge segments defined in Figure 4. The main gauge segment including the neck is between gauge segment lines G4 and G9 (bar 5.2)

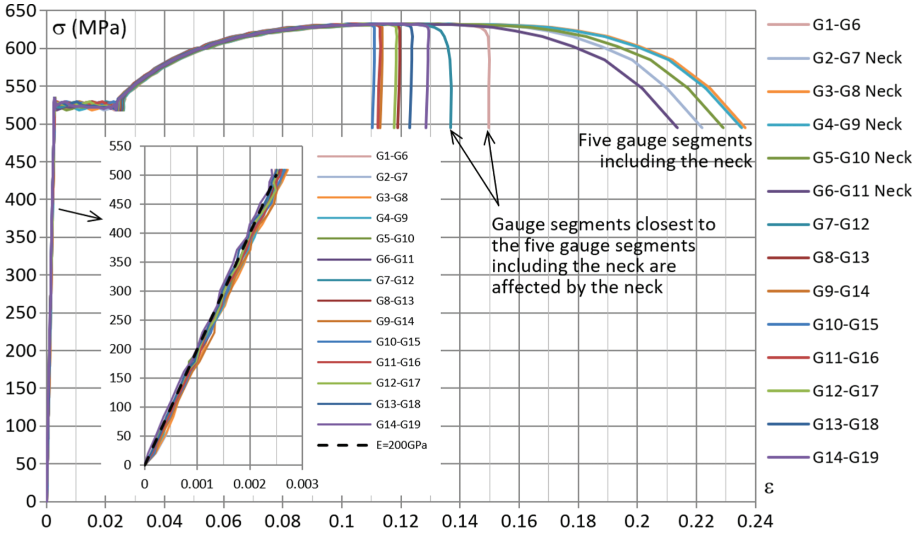

FIGURE 8 Stress–strain curves for all the 5d overlapping gauge segments (fourteen) defined in Figure 5. The inset shows the elastic phase, where the elastic modulus for reinforcement bars according to Eurocode 2, $E = 200$ GPa, is shown with dotted line for comparison (bar 5.2)

By defining gauge segment lines with a 1d (10 mm) distance, the development of the uniaxial strain along the bar can be determined for 5d overlapping gauge segments, as indicated with black arrows in Figure 5. The corresponding stress–strain curves are shown in Figure 8. The elastic range is shown in the inset in Figure 8, which is in good harmony with the elastic modulus for reinforcement bars presented in Eurocode 2, $E = 200$ GPa. Figure 8 shows the variation of the stress–strain curves depending on where the 5d gauge segment is located on the bar.

4.2 | Uniaxial stress–strain curves for 1d, 3d, 5d, and 10d gauge lengths

Figure 9 shows the uniaxial stress–strain curves for bar 5.2 for different gauge lengths: 1d, 3d, 5d, and 10d. The neck is located at the center in each gauge segment except for the 10d gauge length, where the neck is located slightly asymmetrically. The different gauge lengths did not affect the elastic, yielding, and the strain-hardening phases, but a variation of the strain at maximum stress was in the range

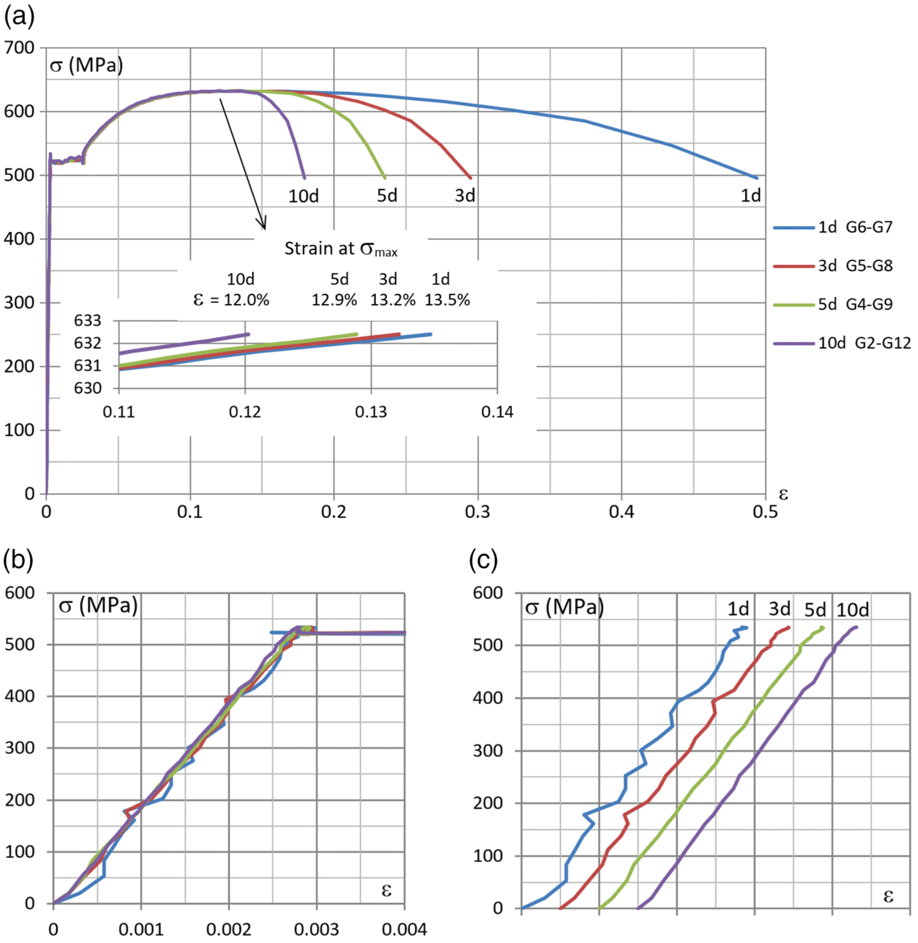

FIGURE 9 (a) Stress–strain curves including the neck for different gauge lengths: 1d, 3d, 5d, and 10d. The elastic curves on (b) have been moved apart on (c) for comparison (bar 5.2)

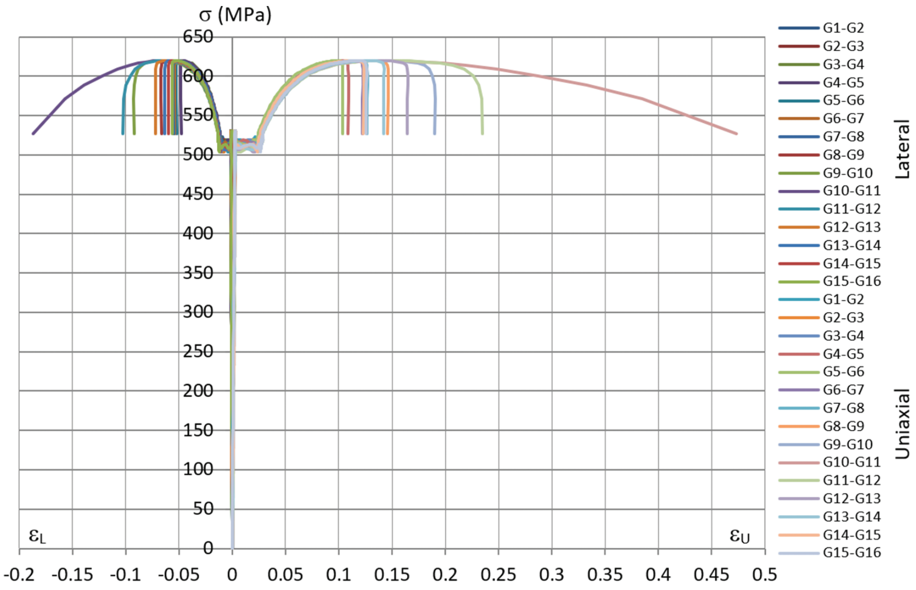

FIGURE 10 Stress–strain graph showing the uniaxial strain (ε_U) on the right horizontal axis (positive as elongation) and lateral strain (ε_L) on the left horizontal axis (negative as contraction), together with the uniaxial tension stress on the vertical axis. The neck is located between G10 and G11. The lateral gauge length was 0.77d and the axial gauge length was 1d (bar 6.3)

$\varepsilon = 12.0$ to 13.5% (inset in Figure 9a). This variation of $\Delta\varepsilon = 1.5\%$ was less than for the 5d side-by-side stress–strain curves in Figure 7, which was $\Delta\varepsilon = 2.4\%$. The reason for this was the effect of the neck zone, which is only included in one segment in Figure 7, but in all sections in Figure 9. After max stress the neck dominated the strain development, which varied greatly.

In the elastic part of the stress–strain curves in Figure 9b the fluctuation was largest for the 1d curves which reduced with increased gauge length, which is natural. The elastic part of the curves in Figure 9c has been moved apart for comparison, which also explains the above-mentioned inaccuracy for the measurement of the lateral strain, which had a gauge length of approximately 0.8d.

4.3 | Uniaxial and lateral stress–strain curves

No standard procedure exists for presentation of the lateral strain for reinforcement bars, but in Figure 10 the lateral strain has been added on the left side of a standard stress–strain curve for uniaxial strain. The curves are identical as they are mirrored about the vertical axis, where the lateral strain is smaller than the uniaxial strain in compliance with the Poisson's ratio. The lateral strain is determined as an average strain of two gauge segment lines, while the uniaxial strain was found between two gauge segment lines (Figure 6). The lateral gauge length was 0.77d and the axial gauge length 1d.

In Figure 11 both the uniaxial and lateral strain development in Figure 10 is now shown as a function of the picture numbers, which is equivalent to showing it as a function of elapsed time during the test. The yielding, which appears as vertical jumps on the strain curves, propagated from right to left (Lüder's behavior), which in Figure 11 appears as a yielding in numerical order, that is, gauge segment G15–G16 was the first to yield and gauge segment G1–G2 was the last to yield. The uniaxial and the lateral strain curves followed each other mirrored about the horizontal axis, where the size difference was in compliance with the Poisson's ratio. It can be seen on the vertical jumps on the

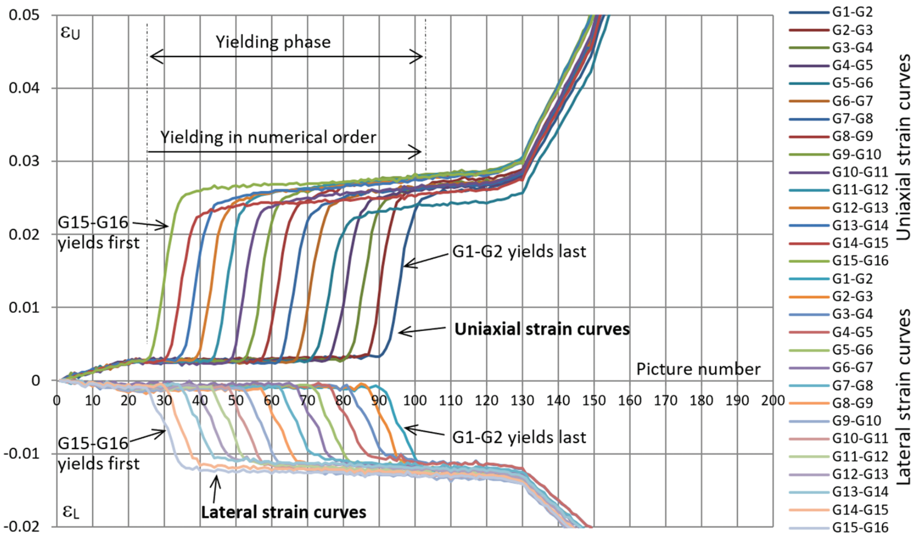

FIGURE 11 Strain development as a function of the picture numbers, where the uniaxial strain (ε_U) is on the upper part of the graph (positive as elongation) and the lateral strain (ε_L) is on the lower part (negative as contraction) (bar 6.3)

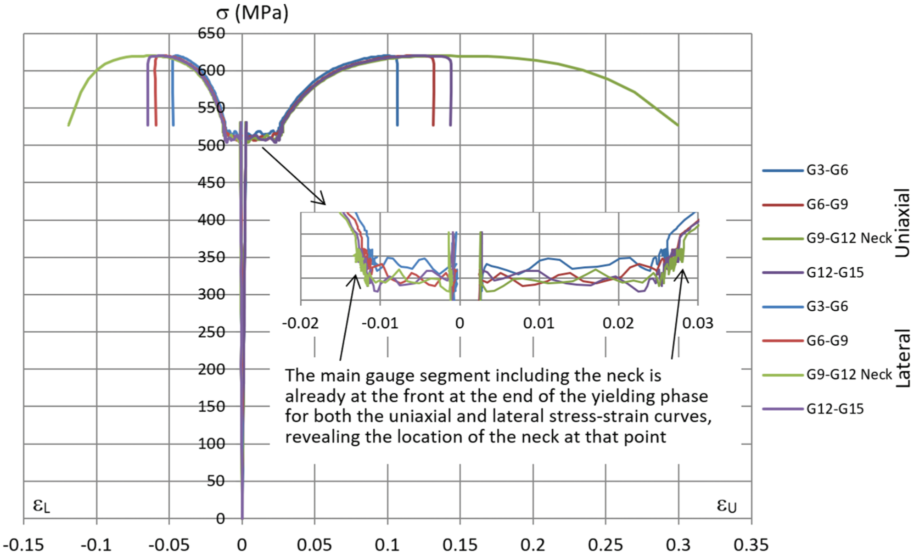

FIGURE 12 Stress–strain curves for four side-by-side 3d gauge segments similar to the 5d gauge segments defined in Figure 4. G9–G12 is the main gauge segment including the neck and is at the front at the end of the yielding phase for both the uniaxial and lateral stress–strain curves (bar 6.3)

strain curves that the bar length that was yielding at any time was approximately 1d.

As discussed in section 4.1, the location of the neck could already be revealed for the uniaxial strain curves at the end of the yielding phase (shown for 5d gauge segments in Figure 7). Side-by-side 3d gauge segments were also sufficient both for the uniaxial stress–strain curves as well as for the lateral strain curves (Figure 12). Stress–strain curves based on 1d, on the other hand, were not as predictive.

4.4 | Lateral strain development

As earlier described, the yielding propagated from one end of the tested bars to the other because of Lüder's behavior and in Figure 13 the development of the lateral strain along the yielding phase is shown as a side view of bar 6.3. The yielding propagated from right to left and the location of the yielding-front can be seen in the graph, as each curve presents the strain situation in the bar. Every second picture no. 24-70 is shown, which cover approximately two thirds of the yielding phase. For example, the curve representing the lateral strain situation at picture no. 70 shows that the yielding front is located between gauge segment lines G6 and G7. The next curve beside it on the right-hand side shows the yielding front when picture no. 68 was taken, etc. This graph shows how regularly the lateral yielding strain propagated along the bar (even distance between the curves) along the yielding phase and it also shows that the bar length that was yielding at any time was approximately 1d.

The development of the lateral strain distribution after the yielding phase for bar 6.3 is shown in Figure 14 for selected pictures marked on the stress–strain curve (red dots). The neck occurred between G10 and G11 and the main 5d gauge segment was between G8 and G13. At the beginning of the strain-hardening phase up to picture no. 150 the lateral strain increased rather uniformly along the bar, but after that the lateral strain in the main gauge segment area increased more rapidly, which can be observed as increased distance between the lines in the graph. The tension stress in the bar was at maximum at picture no. 185 but

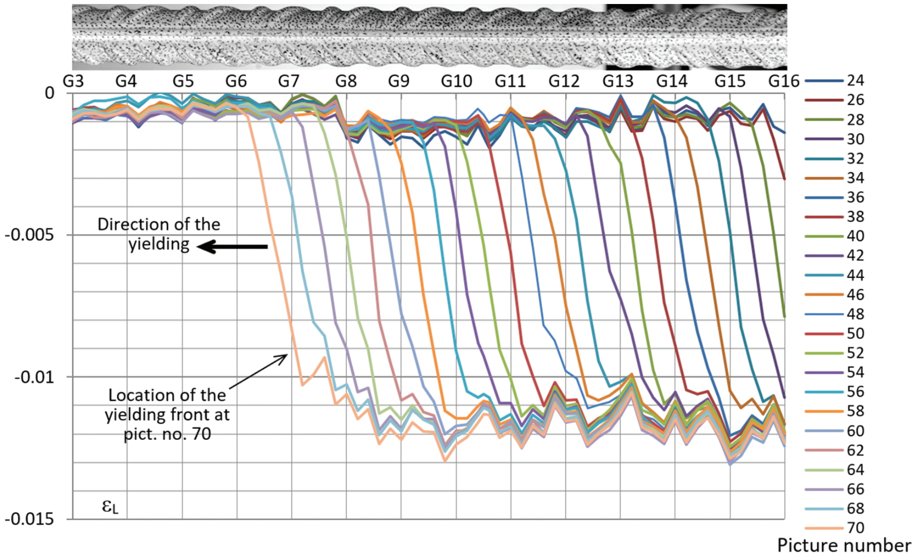

FIGURE 13 Development of the lateral strain as the yielding propagated from one end of the bar to the other (here from right to left) along the yielding phase. Here is every second picture no. 24-70 shown, where the location of the yielding front on picture no. 70 is pointed out. The next curve beside it shows the location of the yielding front on picture no. 68, etc. (bar 6.3)

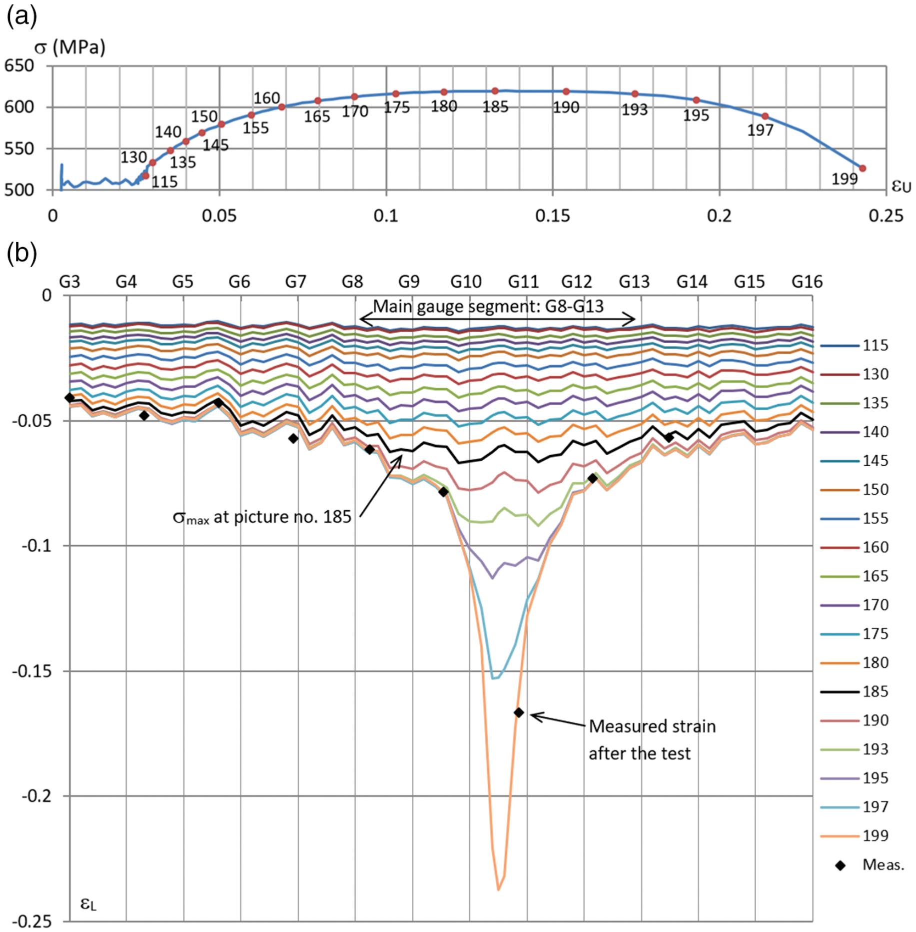

FIGURE 14 (upper graph) A part of the stress–strain curve for the main gauge segment of bar 6.3, that is, between G8 and G13, where selected picture numbers are marked with red dots. (lower graph) Development of the lateral strain distribution (ε_L) along the bar after the yielding phase shown for selected pictures. The lateral strain distribution at max stress is pointed out (picture no. 185). Measured strain with a digital calliper after the test (black dots) is shown for comparison

was rather constant to picture no. 190 when the descending part of the stress–strain curve began for real and the lateral strain was isolated to the neck area. Most of the lateral contraction along the descending phase took place along the main 5d gauge length G8–G13, but in the figure it can be seen that the total affected area was approx. between G6 and G16, that is, 10d.

The width of the bar was measured with a digital calliper both before and after the test at selected locations on the smooth part of the bar (Figure 14). In general, there was good harmony between the strains measured with the digital calliper and the DIC analysis.

5 | POISSON'S RATIO

As described in section 3.2, no standard procedure exists for presentation of Poisson's ratio for reinforcement bars. Poisson's ratio can be analyzed locally for each gauge segment (G1–G2, etc., Figure 6) from the uniaxial and lateral curves

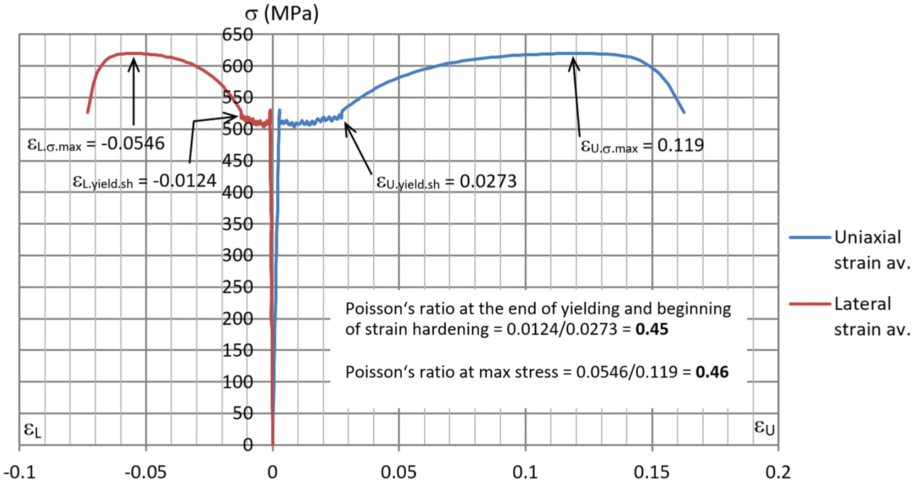

FIGURE 15 The stress–strain graph presents the average uniaxial and lateral strain for all the curves shown in Figure 10, where the Poisson's ratio for two chosen points on the curves was calculated (bar 6.3)

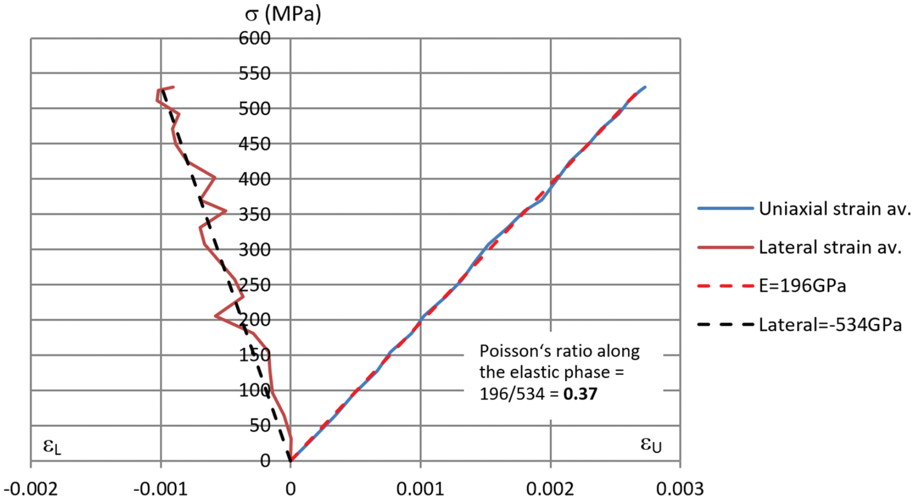

Poisson's ratio along the elastic phase = 196/534 = **0.37**

FIGURE 16 The elastic part of the stress-strain graph in Figure 15, where the Poisson's ratio for the elastic phase was calculated (bar 6.3)

in Figure 10 and it can also be analyzed globally for the whole bar by using the average strains. The average of the stress–strain curves in Figure 10 is shown in Figure 15.

Figure 15 shows the Poisson's ratio at the end of the yielding phase and beginning of the strain-hardening phase as it was calculated (0.45) and also the Poisson's ratio at the max stress (0.46). What happens in the bar after the max stress was isolated at the neck zone and is not of practical interest. The elastic phase of the graph in Figure 15 is shown in another scale in Figure 16.

A linear best fit of the uniaxial strain gave the elastic modulus for the reinforcement bar, which in this case for bar 6.3 was measured at 196 GPa. Similarly, a linear best fit of the lateral strain gave a slope of −534 GPa. The ratio of these two values describes the difference in the strain development of the uniaxial and the lateral strain and therefore also Poisson's ratio (0.37).

Figure 17 presents a graph which shows the development of the Poisson's ratio from the elastic phase all the way to rupture as a function of the picture numbers, together with the tension stress which was scaled down in order to fit into the graph. The elastic part of the curve is shown with a dotted line.

The graph in Figure 17 shows how the Poisson's ratio along the yielding phase gradually increased from the elastic value (0.37) to the value reached at the end of the yielding phase (0.45). This happened gradually when the whole bar was considered, but occurred instantly at the location where the yielding took place. After the yielding phase the Poisson's ratio was more or less constant along the strain-hardening phase up to max stress, that is, constant along the post-yielding phase.

According to Gere and Timoshenko[21] the Poisson's ratio for steel in the elastic phase is normally in the range of 0.27–0.30 and the maximum value of 0.5 is a theoretical upper limit for the Poisson's ratio, which is valid for the plastic phase. For the elastic phase the measured Poisson's values showed greater variation than the above mentioned range which most likely is related to inaccuracy in the DIC analysis due to small deformations in the elastic phase. The post-yielding values, on the other hand, were in good harmony with what was to be expected, as the Poisson's ratio at the end of the yielding phase and beginning of the strain-hardening phase for the reinforcement bars reached values in the range of 0.44–0.49. This was also the case for the smooth bars no. 6.4 and 6.5, which had a yielding plateau like the reinforcement bars. In Table 2 the Poisson's ratio at the end of the yielding phase and beginning of the strain-hardening phase is given for all the tested bars in tests 5 and 6, except for smooth bar no. 5.3 which did not develop a yielding platform (the Poisson's ratio increased gradually from the elastic phase to max stress).

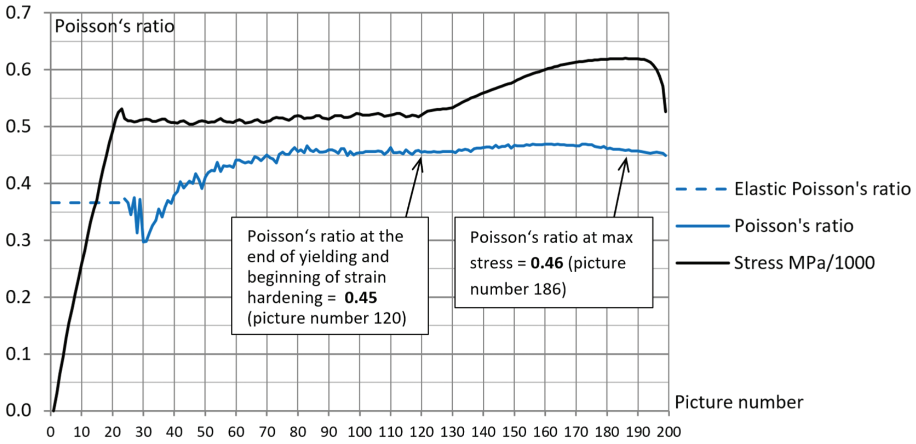

Poisson's ratio at the end of yielding and beginning of strain hardening = **0.45** (picture number 120)

Poisson's ratio at max stress = **0.46** (picture number 186)

FIGURE 17 The development of the Poisson's ratio from the elastic phase all the way to rupture together with the tension stress which was scaled down by a factor of 1,000 in order to fit into the graph (bar 6.3)

TABLE 2 Poisson's ratio for the bars in test 5 and 6 for the main camera

Bar No.	Type	At the end of yielding and beginning of the strain-hardening
5.1	Ribbed	0.48
5.2	Ribbed	0.47
6.1	Ribbed	0.44
6.2	Ribbed	0.49
6.3	Ribbed	0.46
6.4	Smooth	0.44
6.5	Smooth	0.42

6 | CONCLUSIONS

This paper presents measurements of uniaxial and lateral strain of ribbed reinforcement bars with a diameter of 10 mm of class C in accordance with Eurocode 2[18] performed with the non-contact optical technique known as DIC. The bars were all pulled to failure and the development of the uniaxial and lateral strain along the elastic, yielding, strain-hardening, and descending phases was identified. The main findings of this investigation were:

- The optical measuring technique used, DIC, is very suitable for this kind of tests, if caution is taken concerning the surface treatment of the bars and the camera adjustments, stability, and resolution.
- All the ribbed bars developed a yielding plateau where the yielding propagated from one end of the bar to the other (Lüder's behavior). The yielding took place only on approximately a 1d long segment at a time.
- Stress–strain curves determined for different gauge lengths, 1d, 3d, 5d, and 10d, both overlapping and side-by-side, were identical all the way to the maximum stress, but from there the neck formation dominated the strain development.
- There was no connection between the location where the yielding started and the location of the neck.
- The location of the neck could be identified at the end of the yielding phase, where the gauge segment including the neck had reached the maximum strain for both uniaxial and lateral strain. This was possible to identify from stress–strain curves based on 3d or larger side-by-side gauge segments. The neck therefore affected the size of the yielding plateau.
- The Poisson's ratio for the reinforcement bars increased rapidly during the yielding phase to 0.44–0.49 and was more or less constant after that all the way to rupture.

All the initial research questions have been answered. The lateral contraction of reinforcement bars affects the interaction between ribbed reinforcement bars and the concrete, which could result in bond slip and an increase in free length of the bar inside the concrete.

ACKNOWLEDGMENTS

This work was supported by a doctoral grant from the Eimskip University Fund of the University of Iceland, by the University of Iceland Research Fund, and by the Ludvigs Storr Trust Fund.

ORCID

Haukur J. Eiriksson https://orcid.org/0000-0001-9354-2965
Bjarni Bessason https://orcid.org/0000-0002-7963-0763
Runar Unnthorsson https://orcid.org/0000-0002-1960-0263

REFERENCES

1. Chen WF. Plasticity in reinforced concrete. New York, NY: McGraw-Hill, 1980.
2. Pauley T, Priestly MJN. Seismic design of reinforced concrete and masonry buildings. New York, NY: John Wiley & Sons; 1992.
3. Peters WH, Ranson WF. Digital imaging techniques in experimental stress analysis. Opt Eng. 1982;21(3):427–431.
4. Sutton MA, Wolters WJ, Peters WH, Ranson WF, McNeill SR. Determination of displacements using and improved digital correlation method. Image Vis Comput. 1983;1(3):133–139.
5. Lu H, Cary PD. Deformation measurements by digital image correlation: Implementation of as second-order displacement gradient. Exp Mech. 2000; 40(4):393–400.
6. Pan B. Two-dimensional digital image correlation for in-plane displacement and strain measurements: A review. Meas Sci Technol. 2009;20(6):1–17.
7. Tung S-H, Shih M-H, Sung W-P. Development of digital image correlation method to analyse crack variations of masonry wall. Sadhana-Acad Proc Eng Sci. 2008;33(6):767–779.
8. Ghiassi B, Xavier J, Oliveira DV, Lourenco PB. Application of digital image correlation in investigating the bond between FRP and masonry. Compos Struct. 2013;106:340–349.
9. Kurtz S, Balaguru P, Helm J. Experimental study of interfacial shear stresses in FRP-strengthened RC beams. J Compos Construct. 2008;12(3):312–322.
10. Syroka-Korol E, Tejchman J. Experimental investigation of size effect in reinforced concrete beams failing by shear. Eng Struct. 2014;58:63–78.
11. De Wilder K, Lava P, Debruyne D, Wang Y, De Roeck G, Vandewalle L. Experimental investigation on the shear capacity of prestressed concrete beams using digital image correlation. Eng Struct. 2015;82:82–92.
12. Sørensen JH, Hoang LC, Olesen JF, Fisher G. Test and analysis of a new ductile shear connection design for RC shear walls. Struct Concr. 2017;18: 189–204.
13. Melenka GW, Carey JP. Evaluation of fiber reinforced cement using digital image correlation. Plos One. 2015;10(6):e0128644. https://doi.org/10.1371/journal.pone.0128644.
14. Moreira DC, Sphaier LA, Reis JML, Nunes LCS. Determination of Young's modulus in polyester-Al_2O_3 and epoxy-Al_2O_3 nanocomposites using the digital image correlation method. Compos Part A Appl Sci Manuf. 2010;43: 304–309.
15. Gencturk B, Hossain K, Kapadia A, Labib E, Yi-Lung M. Use of digital image correlation technique in full-scale testing of pre-stressed concrete structures. Measurements. 2014;47:505–515.
16. EN ISO 6892-1:2009. Metallic materials—Tensile testing, Part 1: Method of test at room temperature. Brussels, European Committee for Standardization; 2009.
17. LaVision. DaVis 8, Data Acquisition and Visualization software, LaVision GmbH, Anna-Vandenhoeck-Ring, D-37081 Goettingen; 2015. www.lavision.de
18. Eurocode 2. Design of concrete structures—Part 1-1: General rules and rules for buildings. Brussels, European Committee for Standardization; 2004.
19. EN 10080:2005. Steel for the reinforcement of concrete—Weldable reinforcing steel: General. Brussels, European Committee for Standardization; 2005.
20. Fisher JC, Rogers HC. Propagation of Lüder's band in steel wires. ACTA Metallurgica. 1956;4:180–185.
21. Gere JM, Timoshenko SP. Mechanics of materials. 3rd ed. London, Chapman & Hall; 1991.

AUTHOR'S BIOGRAPHIES

Haukur J. Eiriksson
PhD Student
Faculty of Civil and Environmental Engineering, University of Iceland
Reykjavík, Iceland
haukurj@hi.is

Bjarni Bessason
Professor
Faculty of Civil and Environmental Engineering, University of Iceland
Reykjavík, Iceland

Runar Unnthorsson
Professor
Faculty of Industrial Engineering, Mechanical Engineering and Computer Sciences, University of Iceland
Reykjavík, Iceland

How to cite this article: Eiriksson HJ, Bessason B, Unnthorsson R. Uniaxial and lateral strain behavior of ribbed reinforcement bars inspected with digital image correlation. *Structural Concrete*. 2018;19:1992–2003. https://doi.org/10.1002/suco.201800042